Article

Power Scheduling Optimization Method of Wind-Hydrogen Integrated Energy System Based on the Improved AUKF Algorithm

Yong Wang [1], Xuan Wen [2], Bing Gu [1] and Fengkai Gao [1,*]

1 Key Laboratory of Modern Power System Simulation and Control & Renewable Energy Technology, Ministry of Education (Northeast Electric Power University), Jilin 132000, China
2 School of Information Engineering, Nanchang University, Nanchang 330027, China
* Correspondence: fengkaigao@163.com

Abstract: With the proposal of China's green energy strategy, the research and development technologies of green energy such as wind energy and hydrogen energy are becoming more and more mature. However, the phenomenon of wind abandonment and anti-peak shaving characteristics of wind turbines have a great impact on the utilization of wind energy. Therefore, this study firstly builds a distributed wind-hydrogen hybrid energy system model, then proposes the power dispatching optimization technology of a wind-hydrogen integrated energy system. On this basis, a power allocation method based on the AUKF (adaptive unscented Kalman filter) algorithm is proposed. The experiment shows that the power allocation strategy based on the AUKF algorithm can effectively reduce the incidence of battery overcharge and overdischarge. Moreover, it can effectively deal with rapid changes in wind speed. The wind hydrogen integrated energy system proposed in this study is one of the important topics of renewable clean energy technology innovation. Its grid-connected power is stable, with good controllability, and the DC bus is more secure and stable. Compared with previous studies, the system developed in this study has effectively reduced the ratio of abandoned air and its performance is significantly better than the system with separate grid connected fans and single hydrogen energy storage. It is hoped that this research can provide some solutions for the research work on power dispatching optimization of energy systems.

Keywords: AUKF algorithm; integration of wind and hydrogen; UKF; power scheduling

MSC: 68Q25

1. Introduction

With the continuous progress of our society and the development of the economy, the domestic demand for energy is also increasing. The current energy consumption structure has a serious negative impact on environmental protection and the healthy development of the national economy [1]. In particular, coal-based thermal power generation not only causes over-exploitation of coal, but also affects the ecological environment and air quality [2]. Adjusting the existing energy structure is an important measure to promote domestic economic development and improve the ecological environment. At the same time, using renewable energy to replace traditional consumption energy is a way to achieve a safe, economical, and efficient sustainable energy system [3]. The wind-hydrogen integrated energy system is one of the important research directions in the sustainable clean energy system. At present, the utilization method of wind power generation is mainly distributed power generation, which is largely to improve the shortcomings of centralized power generation [4]. Usually, distributed power sources form a micro-grid with multiple systems through topology and act on the main grid. However, there are still many problems in the process of integrating distributed renewable energy into the main power grid, such as

reducing the reliability of the power grid and curtailing wind, affecting the reactive power balance of the power grid, and reducing the quality of the power grid. The emergence of key technologies for hydrogen energy storage has effectively promoted the development of distributed power stations and played a key role in the research of distributed energy, especially in the development of fuel cell technology. The hydrogen fuel is supplied to the gas network, which improves the utilization efficiency of wind energy and promotes the development of the wind hydrogen system [5].

At present, the research work of AUKF has become a main direction in the field of energy system power scheduling research; this technology has also attracted the attention of many domestic and foreign scholars. Zhang et al. [6] proposed a robust adaptive UKF (Unscented Kalman Filter) algorithm, based on a fault detection mechanism for estimating the state of distributed-driven electric vehicles, and designed an estimator based on robust adaptive UKF to estimate longitudinal speed, lateral speed, and sideslip angle. Simulation results show that the robust adaptive UKF algorithm can significantly reduce the estimation errors of the three state variables and is superior to the standard UKF algorithm in terms of accuracy and robustness. Ge [7] proposed the information fusion technology based on AUKF and, combined with Markov distance theory, designed a new AUKF scheme to solve the error problem in nonlinear systems. Simulation results show that the proposed method is effective when the process error and measurement noise covariance vary with time. Loukil et al. [8] evaluated the state of charge by means of the Extended Kalman Filter, Unscented Kalman Filter (UKF), and Volumetric Kalman Filter (VKF) online. The open circuit voltage test (OCV) was used to verify the battery model proposed in the study. The results show that the proposed method has better accuracy and robustness and reduces the computational complexity of the traditional algorithm. Yuan et al. [9] proposed a nonlinear internal state observer based on an adaptive volumetric Kalman filter algorithm for estimating the mass of oxygen and nitrogen inside the cathode of an onboard PEMFC system. The performance of the proposed observer is verified, and the results show that the proposed observer has good convergence and accuracy. Yang et al. [10] used a three-axis accelerometer and a three-axis magnetometer measurement system, established a nonlinear model based on quaternion, and proposed an improved adaptive fading square root unscented Kalman filter to eliminate a vibration disturbances signal. The calculation method of the fading factor is optimized, which ensures the adaptability of the algorithm and reduces the computational complexity. The results show that the method can effectively filter out the interference noise in the attitude measurement sensor and improve the solution accuracy of the attitude parameters of the drilling tool in the case of sudden changes in the measurement environment, so as to ensure the dynamic stability of the borehole trajectory. To better describe systems as dynamic entities in dynamic environments and to characterize FLS measurements, Franchi et al. [11] proposed an adaptive unscented Kalman filter (AUKF) based estimator. The results show that the solution passes offline testing and the estimator's predictive validity is validated with navigational sample data.

Therefore, this research first builds a distributed wind hydrogen hybrid energy system model and, on this basis, proposes the power scheduling optimization technology of wind hydrogen integrated energy system based on AUKF and further studies the AUKF power distribution method to better improve the accuracy of the algorithm system and the practicality of application.

2. AUKF Wind-Hydrogen Integrated Energy System Power Scheduling Optimization Method

2.1. Model Construction of Distributed Wind-Hydrogen Hybrid Energy System

A distributed wind-hydrogen hybrid energy system mainly generates electricity through small and medium-sized wind energy and is connected to the grid locally to reduce wind curtailment, thereby improving the utilization rate of battery power storage and hydrogen storage [12]. When the wind energy is connected to the grid and the power is insufficient, the fuel cell will be used to connect the grid. When there is a surplus of wind

power, the electrolyzer will be used to absorb and store hydrogen to build a wind-hydrogen integrated energy system [13]. To better study the wind power generation system, the direct drive wind turbine is selected as the research object in this study. Compared with the doubly fed wind turbine, the direct driven wind turbine has a large power density, a wide operating range, and is less affected by the frequency range. In terms of mechanical structure, the direct drive type has a multi-stage structure and does not require a speed increase gearbox. The wind power generation system model in this section is based on the process of wind energy utilization, which includes three parts, physical kinetic energy model, transmission shaft model, and electrical system model. Hydrogen energy storage is an energy storage technology with good development prospects at present. "Hydrogen-electricity" and "electricity-hydrogen" conversion devices are used to control wind power and power supply. The system designed in this study is mainly a distributed common DC bus type. The wind-hydrogen hybrid energy structure is shown in Figure 1.
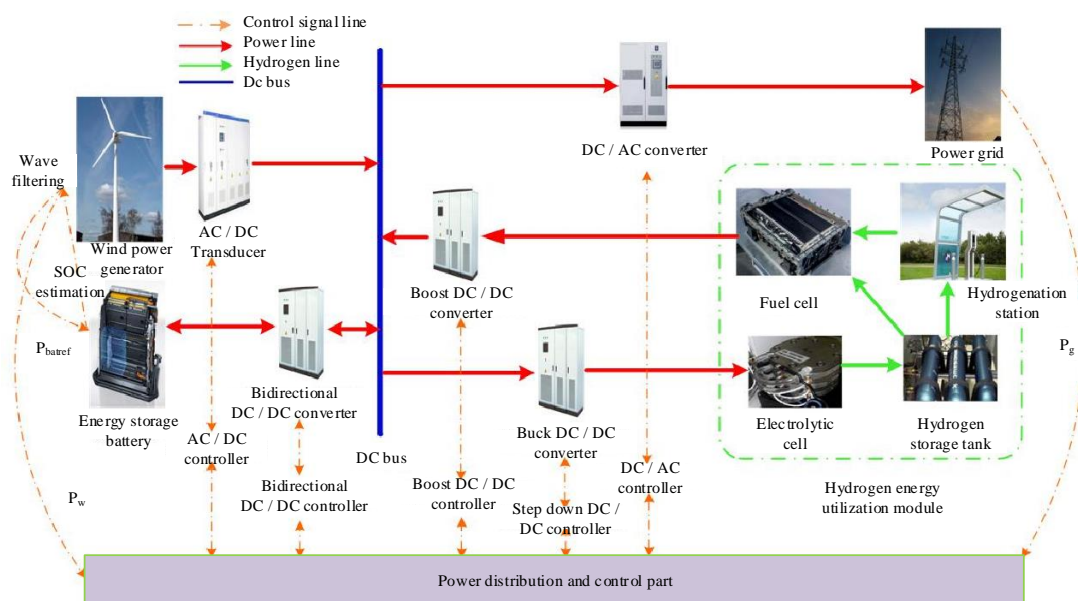

Figure 1. Topology diagram of distributed wind-hydrogen hybrid energy system.

In Figure 1, the Permanent Magent Synchronous Generator (PMSG), Electrolyzer (EL), Fuel Cell (FC), and Battery (Bat) enter the DC bus through the converter. In the energy storage system, the reason for the unbalanced power phenomenon is mainly the dynamic response delay of hydrogen energy storage, which makes the system face the volatility of wind power. This device is used for second-level response operation, assisting EL-FC to perform electric hydrogen-electric cycle operation, so as to ensure that the DC bus can maintain a stable voltage and improve the grid-connected controllability of fans [14]. The stability of the DC bus voltage can only be ensured by keeping the balance of the system's current input and output in the DC capacitor. The calculation of the DC bus capacitor voltage is shown in Formula (1).

$$C_{dc}\frac{dU_{dc}}{dt} = I_{PMSG} + I_{bat} + I_{fc} - I_{el} \tag{1}$$

In Formula (1), C_{dc} represents the DC bus capacitance (F); U_{dc} is DC bus voltage (V); and I_{PMSG}, I_{bat}, I_{fc}, and I_{el} are the currents (A) of PMSG, Bat, FC, and EL, respectively. The system monitors the real-time parameters of each subsystem, allocates power, and operates the control part, so as to judge the current system in real-time and obtain the control signals of each subsystem [15]. When the converter receives the control signal, it assists the system in power distribution to ensure the controllability of the grid-connected power and effectively improve the penetration performance of wind energy.

2.2. Power Dispatching Optimization Technology of Wind-Hydrogen Integrated Energy System

In order to improve the overall accuracy of the model, this study will build the RC link model based on the original Thevenin model, adding the related discipline theory based on polarization resistance and its parallel connection. Set open circuit resistance, polarization internal resistance, and internal resistance as U_{oc}, $R_{pi}(i = 1, 2, 3)$, and R_o, respectively. The charge and discharge current of the battery, the current on the polarization resistance, and the working voltage of the battery are I, I_p, and Ul. According to the parallel theory of polarization resistance and polarization capacitance, the RC link is formed in parallel. Based on the basic circuit laws and BMS design requirements, the circuit formulas (Ul, R_{pi}) of the RC link of the Thevenin model are obtained, as shown in Formula (2).

$$\begin{cases} Ul = U_{oc} + IR_o + U_{pi} \\ U_{pi} = \frac{1}{C_{pi}R_{pi}}U_{pi} + \frac{1}{C_{pi}}I \end{cases} \tag{2}$$

Assume that the on-time calculation formula of BMS is BMS_k, where k is the time constant, and the state quantity of the BMS system is BMS_0; see Formula (3).

$$BMS_k = BMS_0 + \int_0^t \frac{I(t)}{C_N} dt \tag{3}$$

Set the polarization resistance as U_{p1}, U_{p2}, U_{p3}, and select the constant voltage at the battery end in the BMS system as the observation to obtain the observation equation, as shown in Formula (4).

$$[U_{I,k}] = [1\ 1\ 1\ 0] [U_{p1,k}, U_{p2,k}, U_{p3,k}, BMS_k] + [R_o][I_{I,k}] + [U_{oc}] + [v_k] \tag{4}$$

In Formula (4), T_s is the sampling time, C_N is the rated capacity of the battery, $v_k \sim (0, R)$ is the observation noise, and $w_{i,k} \sim (0, Q_i)$ is the system noise, where I in the system noise can be 1–4. The battery data is mostly completed under a different battery state of charge (State of charge, SOC) [16]. Therefore, in order to accurately identify the parameters of different models, the Ultimate Tensile Strength (UTS) sub-capacity cabinet was used for research and analysis; the object was a 3.2 Ah 18,650 lithium battery at a room temperature of 25 °C. The third order Thevenin model is used to analyze the constant current charge and discharge parameters. The model design is shown in Figure 2. Wherein, Figure 2a is the third-order Thevenin model, and Figure 2b is the sampling point diagram of the complete pulse discharge process.
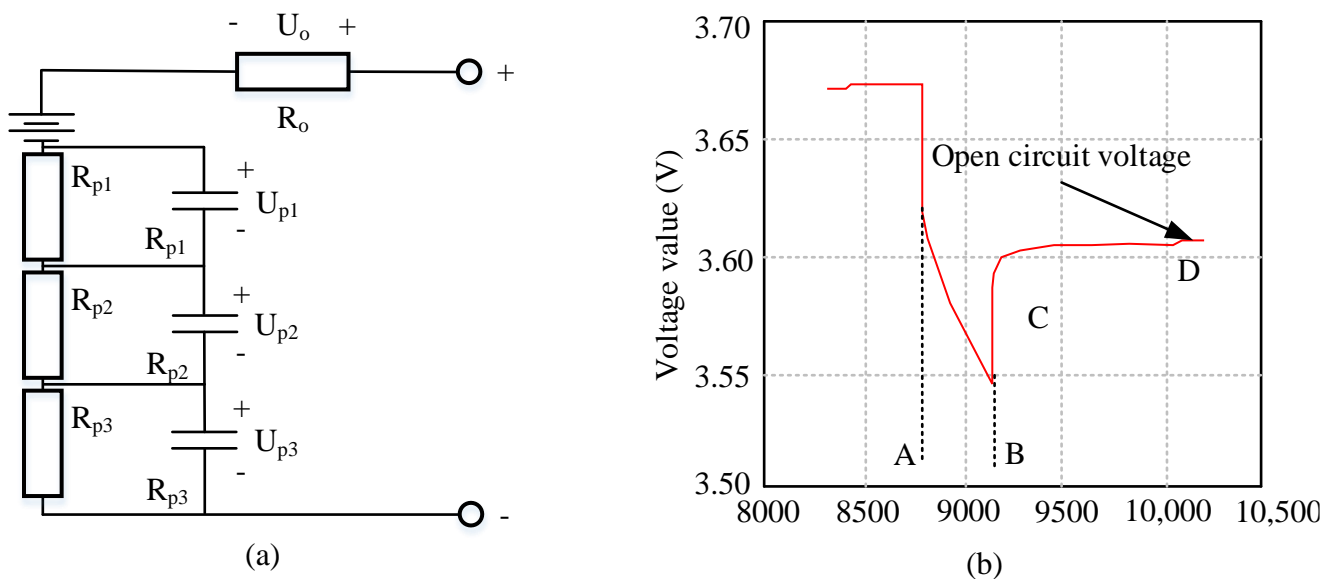

Figure 2. Model and sampling.

The battery charging state of the BMS system is 100.00%. The UTS sub-container set on the UTS sub-capacitor is set to discharge for 6 min (360 s) and then stand for 18 min (1080 s). The discharge pulse current is 0.5 C to ensure that the SOC of the battery decreases by 0.1 each time when it is charged. The experiment was repeated a total of 7 times. Finally, find the functional relationship between open circuit voltage and BMS (SOC) fitted by 7th degree polynomial, as shown in Formula (5). The polynomial fitting functions are all carried out on the basis of Matrix Laboratory (MATLAB) theory [17].

$$
\begin{aligned}
U_{oc} = & -92.4 \cdot BMS^7 + 267.6 \cdot BMS^6 \\
& -436.1 \cdot BMS^5 + 342.9 \cdot BMS^4 \\
& -140.8 \cdot BMS^3 + 26.7 \cdot BMS^2 \\
& -1.78 \cdot BMS^1 + 3.363
\end{aligned}
\tag{5}
$$

In Figure 2, A to B is regarded as the corresponding process of discharge of the polynomial fitting function, and B to D is regarded as the corresponding process of its resting. The BMS at a certain time node of the intercepted 7 polynomial fitting functions is 0.5. In this model, the corresponding active range of the RC network in the zero state is mainly in the A to B area. The starting point is point A. Therefore, according to the equivalent circuit model of the battery, the calculation formula of the voltage (U_{RCi}) in the A–B region can be obtained:

$$
U_{RCi} = IR_p\left(1 - e^{-\frac{t}{R_{pi}C_{pi}}}\right)
\tag{6}
$$

In Formula (6), the value of RC links of different orders is $i = 1, 2, 3$. Similarly, if the parameters of the B–D static area are fitted according to the curve fitting function under the MATLAB theory, the voltage calculation method is shown in Formula (7).

$$
Ut = b_1 \exp[-c_1(t - t_B)] + b_2 \exp[-c_2(t - t_B)] + b_3 \exp[-c_3(t - t_B)] + U_D + b
\tag{7}
$$

However, it should be noted that if it is needed to solve the resistance, capacitance, and internal resistance of the RC link, the calculation formulas of R_{pi} and R_0 should be combined to achieve the parameter fitting, as shown in Formula (8).

$$
\begin{cases}
R_{pi} = \dfrac{b_1}{I\{1 - \exp[-c_1(t_B - t_A)]\}} \\[3mm]
R_0 = \dfrac{b}{I}
\end{cases}
\tag{8}
$$

Finally, R_0, the parameter fitting calculation formula related to the BMS function is obtained, as shown in Formula (9).

$$
\begin{aligned}
R_0 = & -142.46 \cdot BMS^7 + 573.74 \cdot BMS^6 \\
& -826.54 \cdot BMS^5 + 634.99 \cdot BMS^4 \\
& -217.25 \cdot BMS^3 + 90.26 \cdot BMS^2 \\
& -12.56 \cdot BMS^1 + 0.7162
\end{aligned}
\tag{9}
$$

Figure 3a shows the polarization resistance of RC link, and Figure 3b shows the polarization capacitance of RC link. Formula (9) is used as the parameter fitting calculation formula for the function relationship between R_0 and BMS; finally the polarization resistance and capacitance of the RC link under the third order Thevenin model of the constant current charge-discharge experiment can be obtained. From the above Figure 3a,b, the polarization resistance and capacitance $R_{p1}, C_{p1}, R_{p2}, C_{p2}$ of the RC link under the third order Thevenin model are relatively stable from 0.1 to 0.9. However, the R_{p3}, C_{p3} polarization resistance is relatively stable between 0.1 and 0.9, while the polarization capacitance has a relatively large variation in this area. The reason is that the capacitor is a series-mixed structure, which is affected by factors such as leakage and breakdown. It leads to the

abnormality of the equivalent circuit and increases the capacitance loss [18]. In addition, the resistance value of capacitor and DC is infinite, so when leakage or breakdown occur, the DC resistance will decrease.
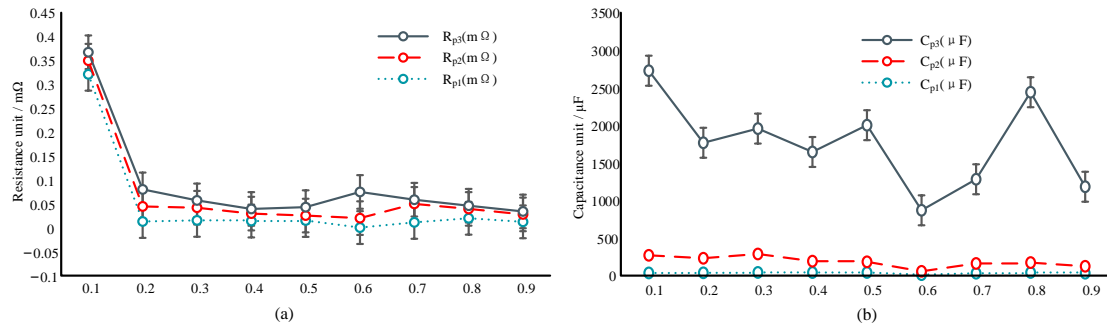

Figure 3. Polarization resistance and capacitance of RC link under the third order Thevenin model.

2.3. Adaptive Kalman Filtering (AUKF) Power Allocation Method

In order to improve the power distribution effect of the model proposed in this study, an unscented Kalman filter (UKF) algorithm is firstly proposed, which is a minimum mean square error estimation algorithm based on unscented transform (UT). UKF improves the adaptive performance of traditional Kalman filtering, ensures the accuracy of sampling, and makes known variables consistent with the distribution of probability density. For real-time estimation of battery SOC, charge and discharge monitoring is required during battery operation. Due to the complex electrochemical reaction causing the estimation error of the SOC value, the error will accumulate. The UKF can be adjusted by SOC and various parameters to reduce the influence of the error, and finally calculate the accurate minimum root mean square estimation result. Therefore, a dynamic equivalent circuit model is constructed according to the UKF principle, and error terms ζ and ξ are introduced at the same time, as shown in Formula (10).

$$\begin{cases} soc_{j+1} = h(soc_k, i_k) \\ U_{j+1} = g(soc_k, i_k) \end{cases} \tag{10}$$

where i_k represents three-phase power supply current. Formula (10) is used as the state measurement formula of UKF, and the UKF gain also plays a decisive role in SOC correction. In order to improve the anti-interference of non-Gaussian nature. The errors of SOC and terminal voltage exist in the state vector. Therefore, x_{k-1} is set as the extended state vector and P_{k-1}^x is the covariance, so the SOC estimation method is shown in Formula (11).

$$\begin{cases} x_{k-1} = \begin{bmatrix} soc_{k-1} & 0 & 0 \end{bmatrix} \\ P_{k-1}^x = \begin{bmatrix} P_{k-1} & 0 & 0 \\ 0 & \zeta' & 0 \\ 0 & 0 & \xi' \end{bmatrix} \end{cases} \tag{11}$$

In Formula (11), $k = 1, 2, \ldots, \infty$, ξ' and ζ' represent the covariance of the error terms ζ and ξ.

The application of UKF in SOC estimation is the capacity waveform of a fully charged battery discharged at a rate of 1 C. The whole discharge time is 4150 s, with four discharges of 1000 s successively and an interval of 50 s. The SOC estimation algorithm proposed by the model is used to estimate the experimental data. Extended Kalman filter (EKF) is widely used in battery estimation. The initial SOC is based on the UKF algorithm and the standard covariance of the actual value and the initial SOC is 0.1. At the beginning of discharge, a UKF-based algorithm can well estimate the real SOC curve but an EKF-based method cannot estimate the real value of SOC. This shows that EKF is more dependent on the initial value and UKF's algorithm converges faster. In the middle of discharge, the

estimation effect of EKF and UKF algorithm is similar. However, at the end of discharge, the EKF algorithm fluctuates greatly and cannot estimate the battery SOC value very well. The same problem does not exist in the UKF algorithm. The fast convergence rate of UKF shows that it is more suitable for nonlinear systems than EKF.

Because the filtering technology in the current project can only perform the power distribution of a specific frequency band, it has certain limitations in application. Additionally, the power input value also has a certain influence on the phase delay and is difficult to meet the grid connection requirements in the application project. Therefore, this study proposes a power allocation method based on AUKF, as shown in Figure 4.
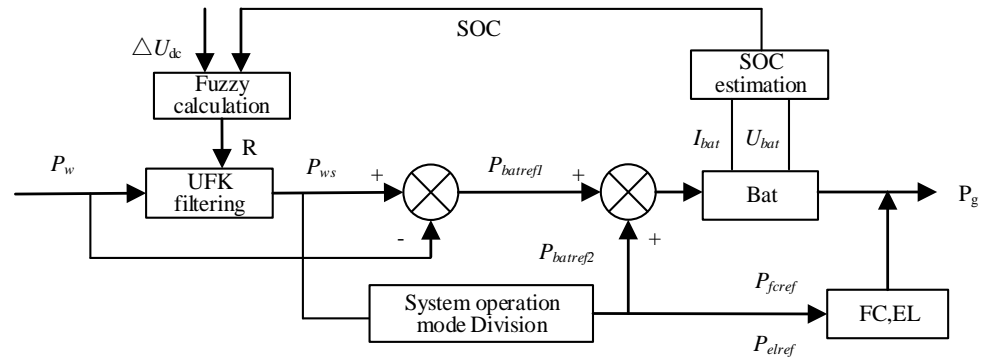

Figure 4. AUKF filter control diagram.

The output power of the fan without the intervention of the energy storage system is expressed as P_w and the smoothed output power after filtering is expressed as P_{ws}. The output power of the wind turbine is obtained after the intervention of the AUKF and represented by P_{ws}. The difference between the output power and the smoothed power is expressed as the fluctuating power of the battery $P_{batref1}$. P_{ws} obtains the power values of EL, FC, and Bat through system operation, which are P_{elref}, P_{fcref}, and $P_{batref2}$, respectively. Among them, $P_{batref2}$ represents the power imbalance caused by the delayed response of FC and EL in the process of hydrogen energy storage, i.e., $P_{batref} = P_{batref1} + P_{batref2}$. When the SOC value is close to the limit, the SOC estimation and the change of the DC bus voltage can indicate the filtering ability of the UKF, so that the SOC value is within the safe range to meet the grid-connected power P_g requirements of the grid.

In practical engineering, if the grid-connected power is not properly limited, when the wind speed is too large, fluctuations in the DC bus voltage will occur, which easily lead to deep charge and discharge. Therefore, the fuzzy control is integrated into the UKF to monitor the SOC and DC bus voltage changes in real time and achieve the power distribution effect based on the AUKF. The SOC is selected as the fuzzy variable, and the input of the model control quantity is selected as the change of the bus voltage relative to the reference value, so as to ensure the stability of the DC bus and ensure the power smoothing performance of the hydrogen energy storage device. The target value calculation of the extension smooth output is shown in Formula (12).

$$
\begin{cases}
p_k^{y-} = \sum_{i=0}^{2L} w_i^{(c)} (Pw_{i,k|k-1} - P_{wk}^-)(Pw_{i,k|k-1} - p_{wk}^-) + \varphi R(k+1) \\
K_k = p_k^{xy} (p_k^{y-})^{-1} \\
(P_{ws})_{k|k} = (\hat{P}_w)_{k|k-1} + K_k[(P_w)_k - (\hat{P}_w)_{k|k-1}]
\end{cases} \tag{12}
$$

The value of the measured covariance R in UKF affects the smoothing effect of the wind power, that is, when the value of R is small, the change of the measurement equation will have a significant impact on the filtering effect. When R is large, it can cope with wind speed and sudden change of bus voltage. When the change of DC bus is positive, the energy storage system should be in the charging state; otherwise, it should be in the

discharging state. The range of battery SOC is considered through fuzzy logic control. When the battery SOC is high and in the charging state or the battery SOC is low and in the discharging state, the target output power of the battery can be changed by reducing R, the difference between the smooth value and the wind power; thus, the power borne by the battery can be reduced. When the SOC of the battery is high and in the discharge state or the SOC of the battery is low and in the charge state, increase R; thus, the power borne by the battery is increased. This can slow down the overcharge and overdischarge of the battery under extreme conditions and can effectively improve the battery life. The difference between the filtered smooth power and the grid load is borne by EL and FC.

As a whole, the distributed wind-hydrogen hybrid system decomposes and coordinates different energy forms in production, transmission, consumption, etc. At the same time, it takes time, space, multiple constraints, and utilization efficiency into account, including the overall coordination and power distribution of the system. In this paper, the grid load is used as the objective function of the system, as shown in Formula (13), to change the nonadjustable generation characteristics of renewable energy.

$$\min f = \sum_{t=t_0}^{T} \left| P_{ws} - P_g + P_{fc} - P_{e1} + P_{bat} \right| \tag{13}$$

In Formula (13), $P_{w\min} \leq P_w \leq P_{w\max}$, $0 \leq P_{fc} \leq P_{fc\max}$, $0 \leq P_{el} \leq P_{el\max}$, $p_{t\min} \leq p_t \leq p_{t\max}$, $U_{dc\min} \leq U_{dc} \leq U_{dc\max}$. $P_{w\min}$, $P_{w\max}$ respectively represent the lower limit and upper limit of the extension power P_w (W). $U_{dc\min}$ and $U_{dc\max}$ represent the lower limit and upper limit of DC bus voltage U_{dc} (V), respectively. $p_{t\min}$ and $p_{t\max}$, represent the lower limit and upper limit of the hydrogen storage tank pressure P_t (kpa). $P_{el\max}$ represents the fuel cell power (W). $U_{dc\max}$ represents the power of the electrolyzer (W).

For the battery energy storage constraint, in addition to considering the SOC operating range, the constraint of charging and discharging times is added. Although the operating range of the battery SOC has been optimized, the limit value of SOC is still a constraint for the safe operation of the battery. The main constraints of the energy storage battery are shown in Formula (14).

$$\begin{cases} P_{bat} \leq Pbatrate \\[2mm] SOC_{\min} \leq SOC \leq SOC_{\max} \\[2mm] \sum\limits_{t=0}^{n\Delta T} U_{kch} < K_{ch} \\[2mm] \sum\limits_{t=0}^{n\Delta T} U_{dis} < K_{dis} \end{cases} \tag{14}$$

In Formula (14), ΔT is the period long term and n is the number of periods. K_{dis}, K_{ch}, U_{kch}, and U_{dis} respectively represent the limit value of battery charge and discharge times and the battery charge and discharge times in a certain period of time.

The system model is further divided into different modes to allow the battery to compensate for the delay characteristics of hydrogen energy. According to the grid-connected power and load requirements, let the net power be P_{se}, then $P_{se} = P_{ws} - P_g$. If $P_{ws} < P_g$, then $P_{se} < 0$, it means low wind speed; if $P_{ws} > P_g$ so $P_{se} > 0$, means high wind speed. For the P_{ws} allocation in the energy storage system model, the pressure of the hydrogen storage tank is used as the mode division basis, four modes can be obtained and the final output power of FC, EL, and Bat can be calculated.

When $P_{se} < 0$, the electrolyzer was out of operation and the model was the lack of power. The operating state of FC and Bat was selected by the pressure of the hydrogen storage tank. Mode 1: When the battery is completely supplied with the insufficient power,

the SOC is too low and in extreme conditions the battery can be decommissioned. The reference power calculation is shown in Formula (15).

$$
\begin{cases}
P_{elref} = 0 \\
P_{fcref} = 0, \ p_t \leq p_{tmin} \\
P_{batref2} = \begin{cases} P_{se}, SOC \geq SOC_{min} \\ 0, SOC \geq SOC_{min} \end{cases}
\end{cases}
\tag{15}
$$

Mode 2: If P_{se} is equal to the FC power, that is, P_{se} less than the maximum power of the FC, then the Bat is affected by the FC delay, which will cause the unbalanced power of the system. See Formula (16) for the reference power calculation.

$$
\begin{cases}
P_{elref} = 0 \\
P_{fcref} = \begin{cases} P_{fcmax}, P_{tmin} < p_t \cap |P_{se}| \geq P_{fcmax} \\ |P_{se}|, p_{tmin} < \cap |P_{se}| < P_{fcmax} \end{cases} \\
P_{batref2} = \begin{cases} P_{se} + P_{fc}, SOC_{min} \leq SOC \leq SOC_{max} \\ 0, SOC < SOC_{min} \cup SOC > SOC_{max} \end{cases}
\end{cases}
\tag{16}
$$

When $P_{se} > 0$, the fuel cell was out of operation, the system model still had residual power, and the operating state of FC and Bat was selected by the pressure of the hydrogen storage tank.

Mode 3: When the EL operation is affected by the high pressure of the hydrogen storage tank, the Bat absorbs all the remaining power. When the SOC is too high, and in extreme conditions, the battery can be de-operated. The reference power calculation is shown in Formula (17).

$$
\begin{cases}
P_{fcref} = 0 \\
P_{elref} = 0, \ p_t \leq p_{tmax} \\
P_{batref2} = \begin{cases} P_{se}, SOC \leq SOC_{max} \\ 0, SOC > SOC_{max} \end{cases}
\end{cases}
\tag{17}
$$

Mode 4: If P_{se} is less than the EL power, that is, P_{se} is less than the maximum power of the EL, then the Bat is affected by the EL delay, which will cause the unbalanced power of the system. See Formula (18) for the reference power calculation.

$$
\begin{cases}
P_{fcref} = 0 \\
P_{elref} = \begin{cases} P_{elmax}, P_t < p_{tmax} \cap P_{se} \geq P_{elmax} \\ P_{se}, p_t < p_{tmax} \cap P_{se} < P_{elmax} \end{cases} \\
P_{batref2} = \begin{cases} P_{se} + P_{el}, SOC_{min} \leq SOC \leq SOC_{max} \\ 0, SOC < SOC_{min} \cup SOC > SOC_{max} \end{cases}
\end{cases}
\tag{18}
$$

3. Verification and Analysis of Power Dispatching Optimization of Wind Hydrogen Integrated Energy System

3.1. Grid-Connected Simulation When the Wind Turbine Is Connected to the Grid Alone and the Battery Is Only Filtered

In order to verify the AUKF power allocation strategy, this section establishes the above system model based on the MATLAB/simulink platform. The simulation uses the real wind speed data and average load data of a wind farm. In order to meet the repeatability and accuracy of the results, the simulation arrangements are as follows: (1) First, conduct the simulation when the fan is connected to the grid separately and provide the tracking of other parameters of the fan. (2) In order to verify the compensation

effect of the battery on the delay characteristics of the hydrogen energy device, the simulation is carried out for the case that the battery only filters and does not bear the unbalanced power generated by hydrogen storage. (3) In order to verify the effectiveness of the strategy in this paper, in the simulation, in order to extend the battery life, the operating range of the battery SOC is set to 0.2–0.8. Therefore, the initial value SOC0 of the battery SOC is set to 0.2 and 0.8 to compare the results. Finally, the voltage fluctuation of DC bus is given.

First, the estimated and reference values of battery terminal voltage and SOC are analyzed, as shown in Figure 5. Wherein, Figure 5a shows the estimated value and reference value of battery terminal voltage, and Figure 5b shows the estimated value and reference value of SOC. Under the influence of noise, the accuracy of the voltage prediction values under the above three algorithms during battery operation fluctuates slightly. The estimated value of the improved AUKF algorithm is very close to the estimated value of the UKF algorithm and is relatively far from the estimated value of the PF algorithm, suggesting that the BMS estimation model based on the improved AUKF algorithm is more accurate. From the perspective of SOC estimation, compared with the UKF algorithm and PF algorithm, the improved AUKF algorithm has higher prediction accuracy for SOC estimation.
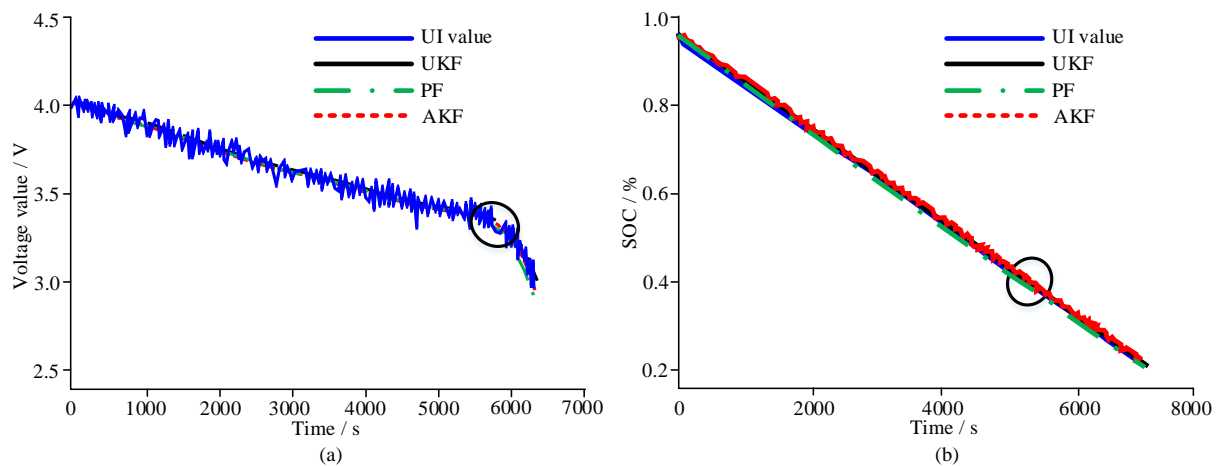

Figure 5. Estimated and reference values of battery terminal voltage and SOC

A separate grid-connected simulation is carried out through the fan parameters. The grid load demand power and grid-connected power are shown in Figure 6. It can be seen from Figure 6 that there is a big difference between the power demanded by the grid load and the grid-connected power. Additionally, the requirements for the system distribution control performance are high. These two curves can judge the stability and security of the system effectively. In 0–2.0 min, 2.2–4.6 min, 11.7–14.1 min, and some other time periods, high-power loads were put into use without energy storage equipment, and the phenomenon of power shortage occurred. At 7.1–8.2 min, the wind speed changed greatly but the load power did not fluctuate. At this time, there was a large residual power in the system. After 13.9 min, the system load demand is less, and there is also a large residual power. Therefore, load changes and sudden changes in wind speed seriously affect the stability of the system power, resulting in unstable operation of the power grid. When the wind turbine is connected to the grid alone, the tracking results of parameters such as dq-axis current and torque show that the wind turbine has a better operation effect.
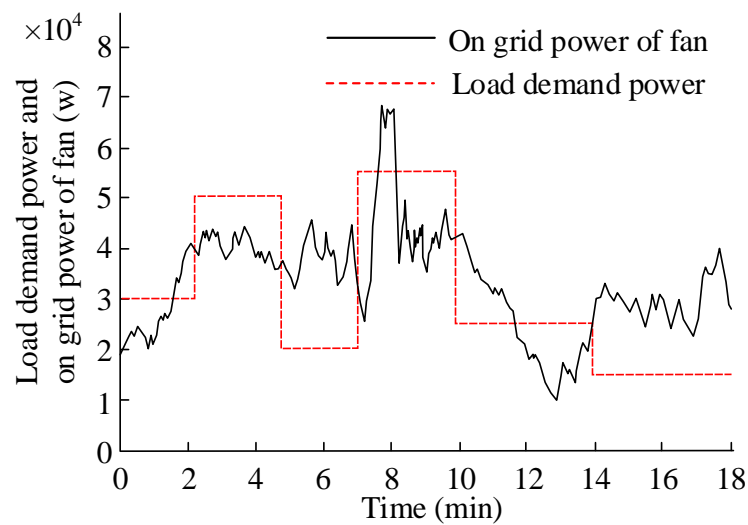
Figure 6. Comparison diagram of load demand and grid connected power of wind turbine.

When the same load demand and wind speed are the same, the grid-connected power of the system after the hydrogen energy device is added to the system as Figure 7. Wherein, Figure 7a shows SOC_0 are 0.2 and Figure 7b shows SOC_0 are 0.8. The battery only needs to bear the fluctuating power of AUKF and does not compensate the delay strategy of FC and EL. When the values of SOC_0 are 0.2 and 0.8, the grid-connected power of the system is much smaller than the individual grid-connected power of the fans. When the value of SOC_0 is 0.8, the stability of grid-connected power is poor, mainly because the system discharge and battery capacity are limited, so that the system absorbs less fluctuating power, thus improving the instability of grid connected power (>0.2). Usually, the system is affected by the pressure of the hydrogen storage tank and the response delay of the hydrogen energy storage, so that the grid-connected power of the system is continuously affected. From the results in Figure 7, it can be seen that the difference between the on-grid power of the wind turbine and the load demand of the grid can be effectively compensated by the battery, and the delay characteristic causes that when the SOC_0 is 0.8 and 0.2, there are surplus power (7.1min) and shortage power (7.9min) respectively, reflecting the weak ability of EL and FC to respond to changes in wind speed.
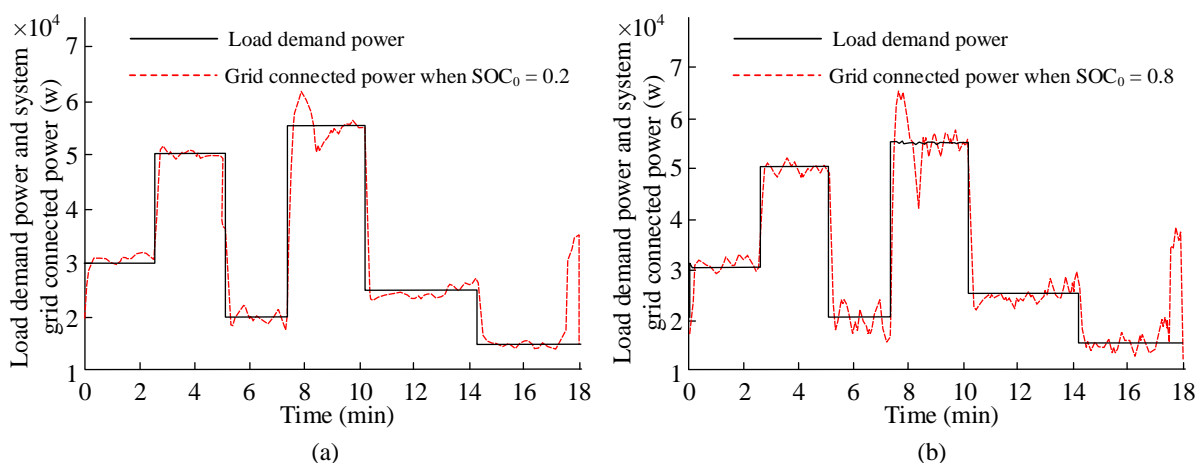

(a)　　　　　　　　　　　　　　　　　　　　　　　(b)

Figure 7. Grid connection of hydrogen energy storage under different conditions.

3.2. Grid-Connected Simulation of Battery Filtering and Delay Compensation

To verify the ability of the adaptive UKF power allocation strategy, this section establishes the above system model based on the MATLAB/simulink platform. The simulation uses the real wind speed data and average load data of a wind farm. In the same simulation

environment, the grid-connected power time curve of the system is shown in Figure 8. The results show that, when the SOC_0 is 0.8 and 0.2, the system can continuously and stably track the load demand of the grid connected power, so that the system operates in dynamic balance. Additionally, the power distribution meets the load demand of the grid connected power, with strong stability, which is better than the independent hydrogen storage system.
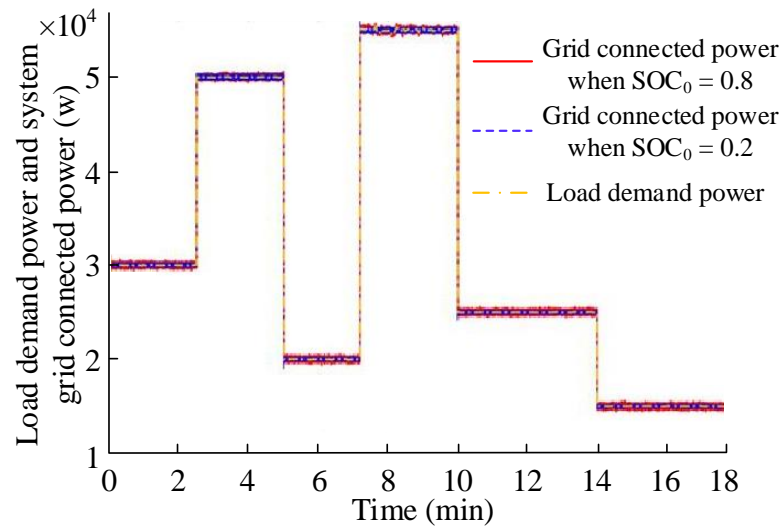

Figure 8. Load demand power and system grid connected power.

The FC and EL power change curves in the whole simulation time period are shown in Figure 9. Wherein, Figure 9a shows FC SOC_0 are 0.2, Figure 9b shows FC SOC_0 are 0.8, Figure 9c shows EL SOC_0 are 0.2, Figure 9d shows EL SOC_0 are 0.8. In Figure 9a, when the SOC_0 is 0.2, the FC start-up is lower than the required time limit. The fuel cell is operated at 0 min, 2.49 min, 7.21 min, etc. Due to the large density of hydrogen, the throughput time of the power grid is extended, so that the FC delays. In Figure 9b, when the SOC_0 is 0.8, the fuel cell is operated at 0 min, 2.49 min, 7.21 min, etc., and the SOC is high; the battery needs to bear more power shortage to reduce the SOC. So, FC is burdened with lower vacancy power. Within 2 min after the system is running, the battery power is lower than Figure 9a and the slope is too large. Figure 9a is consistent with the highest power in Figure 9b, indicating that the system is in a safe operating state when the system is operating to an intermediate period. In Figure 9c, when the SOC_0 is 0.2, at 1.95 min, 5.04 min, 7.89 min, etc., there is residual power in the system. The electrolytic cell cannot track in real time, resulting in unbalanced power. At 17.4–18.1 min, the pressure of the hydrogen storage tank is the highest and the EL return delay is delayed. In Figure 9d, when the SOC_0 is 0.8, the power absorbed by the battery is relatively low, so the power burden of the electrolytic cell is relatively large during this period. When SOC_0 is 0.8, the electrolytic cell has been put into operation for 1.8 min, which is affected by the fuel cell operation delay. At this time, the EL power increases from 0 to 1.02 kW, which is higher than the corresponding position (0.84 kw) in Figure 9c. At the same time, the power values are higher than the corresponding position power in Figure 9c at 5.8 min, 7.8 min, 10.0 min, and 13.9 min. The change of electrolytic cell power at other times is affected by SOC and bus voltage state.
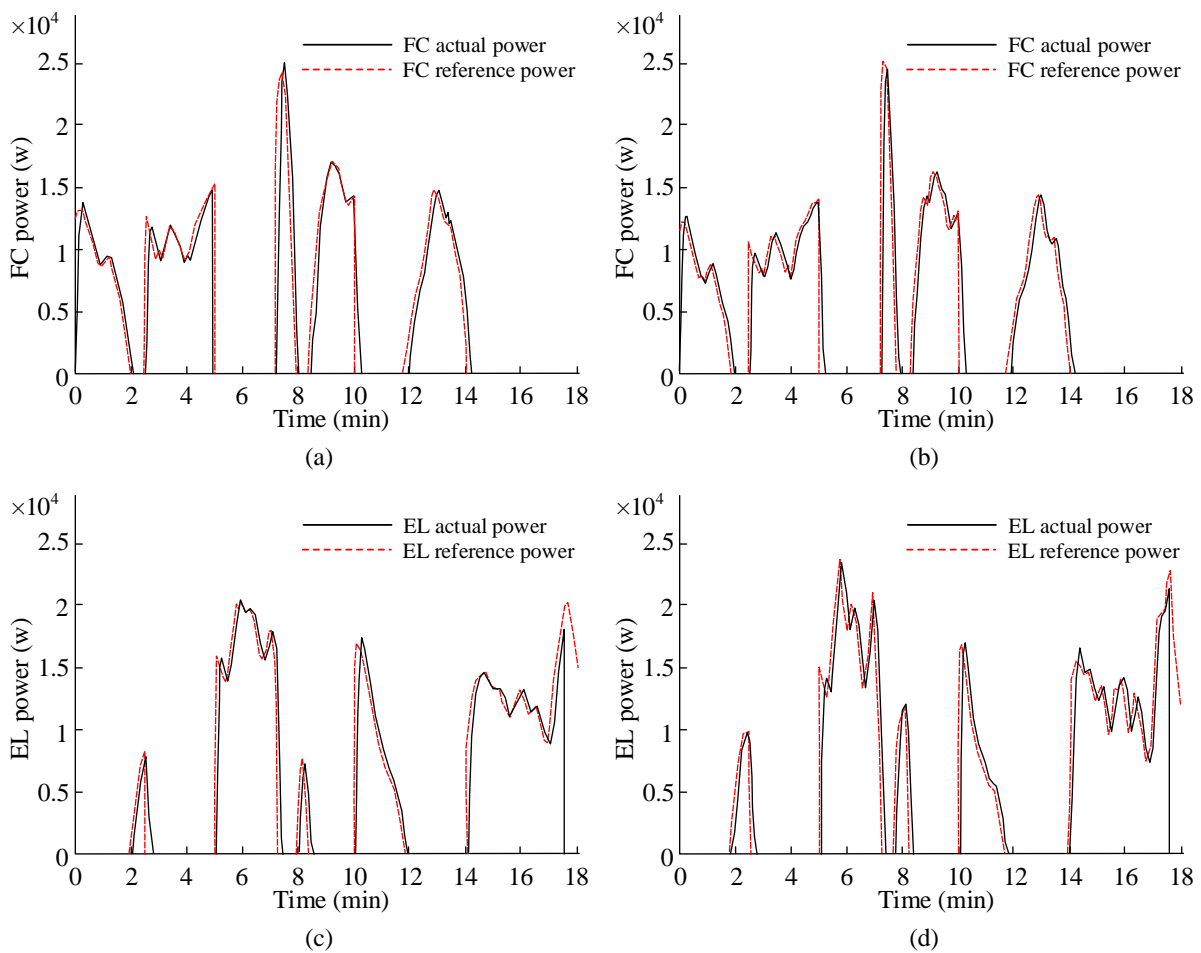
Figure 9. FC and EL power change curve.

The power borne by FC and EL is relatively smooth after filtering, which can prolong the service life of system equipment. The research and analysis show that when the SOC_0 is 0.2, the hydrogen storage tank pressure of the system is too large after 4.8 min, which will cause the battery to return; the SOC will return in about 17.6 min in any case. This shows that the fuel cell plays a role in the system's remaining power and shortage power; however, the gap between the minimum and maximum power is small, so the allocation strategy proposed in this study will not further increase the equipment capacity.

The SOC curve of the energy storage battery changes, as shown in Figure 10. Wherein, Figure 10a shows SOC_0 are 0.2, Figure 10b shows SOC_0 are 0.8. When the SOC_0 is 0.2, the battery is charged and discharged only through the system's remaining and lacking power. The overdischarge phenomenon occurs in 7.2–10.3 min, when SOC is 0.179. After adopting the security strategy, the SOC value remains above 0.2. When the SOC_0 is 0.8, the battery is at the upper limit critical value, the SOC rises rapidly, and the SOC value reaches 0.85 after 18 min. After adjustment by the security policy, the SOC value remains below 0.8.
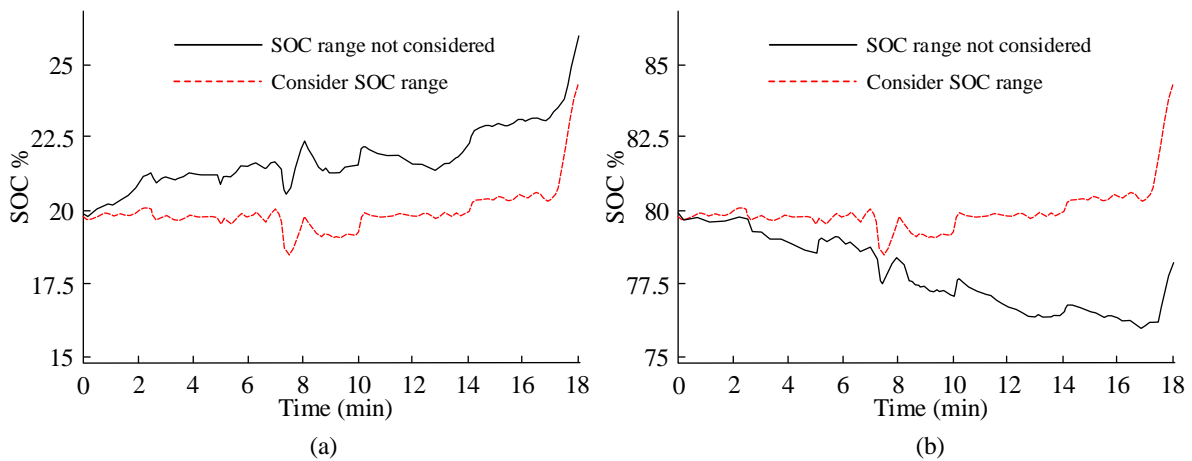
Figure 10. Battery SOC change curve.

Then, the influence of the method proposed in this study on the DC bus voltage of the system is analyzed, as shown in Figure 11. Wherein, Figure 11a represents the change curve of DC bus, Figure 11b represents the change curve of reactive power, and Figure 11c represents the change of DC bus under different algorithms. The results show that under the action of the PI controller, the DC bus voltage and reactive power curves are basically consistent with the reference values. When the SOC_0 is 0.8 and 0.2 and the wind speed changes greatly, the DC bus voltage of the system can be stabilized at 800 V, which has strong stability, reflecting that the proposed distribution strategy can slow down the overcharge and discharge of the battery and also stabilize the voltage of the DC bus. Figure 11c shows the voltage curve of the DC bus obtained by different algorithms. The stability in the period of 7.1–9.7 min is small. Therefore, if the adaptive control method is not used, the performance of the KF filter and the first-order low-pass filter algorithm is poor. This leads to the large fluctuation of the DC bus, which has a great impact on the safe operation of the power grid.
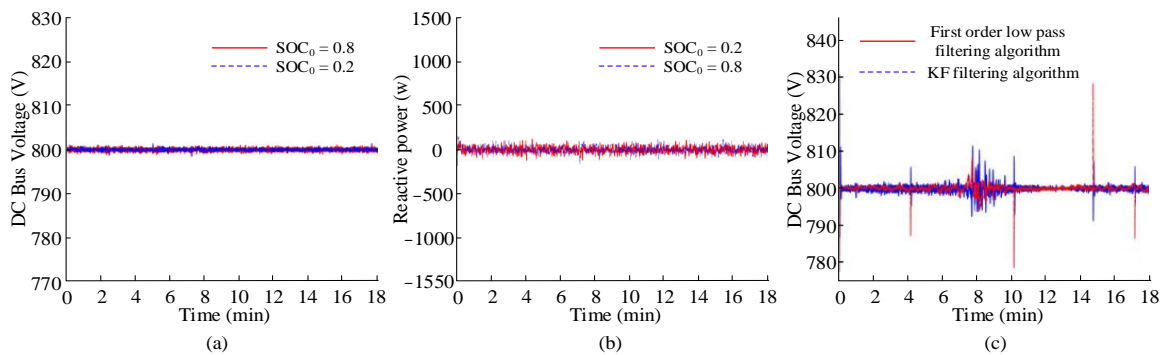

Figure 11. FC and EL power change curve.

4. Conclusions

To solve the power dispatching optimization problem of the wind-hydrogen integrated energy system, this research constructs a distributed wind-hydrogen hybrid energy system model, proposes the power dispatching optimization technology of the wind-hydrogen integrated energy system, and finally constructs a power allocation strategy based on the AUKF algorithm. The results show that when SOC_0 is 0.8 and 0.2, when the wind speed changes greatly, the DC bus voltage of the system can be stabilized at 800 V. The system can obtain continuous and stable tracking of grid connected power on load demand, which makes the system operate in dynamic balance, and the power distribution meets the load demand of grid connected power; reflecting that the proposed distribution strategy can slow down the overcharge and overdischarge of the battery and also stabilize the DC bus

voltage. It is superior to the independent hydrogen energy storage system. When the SOC_0 is 0.2, the battery is charged and discharged only through the system's remaining and lacking power. The overdischarge phenomenon occurs between 7.2 and 10.3 min, when the SOC is 0.179. After adopting the security strategy, the SOC value remains above 0.2. When the SOC_0 is 0.8, the battery is at the upper limit critical value, the SOC rises rapidly, and the SOC value reaches 0.85 after 18 min. After the adjustment of the safety strategy, the SOC value is kept below 0.8. The DC bus voltage curve obtained by using different algorithms is less stable in the 7.1–9.7 min period, so the method proposed in this study can meet the grid connection power requirements and the expected goal of smoothing the power of hydrogen energy devices. However, this paper only conducts simulation, lacks hardware support, and directly determines the system configuration based on the difference between wind power and load. The capacity optimization simulation verification of the simulation system will become a new topic in the next step.

Author Contributions: Conceptualization, Y.W.; methodology, Y.W.; software, Y.W. and X.W.; validation, Y.W., X.W. and B.G.; formal analysis, Y.W. and B.G.; investigation, Y.W. and B.G.; resources, F.G.; data curation, X.W. and F.G.; writing—original draft preparation, Y.W.; writing—review and editing, Y.W. and X.W.; visualization, X.W.; supervision, B.G.; funding acquisition, X.W. All authors have read and agreed to the published version of the manuscript.

Data Availability Statement: The data used to support the findings of this study are available from the corresponding author upon request.

Conflicts of Interest: The authors declare no conflict of interest.

References

1. Gallego, A.J.; Sánchez, A.J.; Berenguel, M.; Camachoa, E.F. Adaptive UKF-based model predictive control of a Fresnel collector field. *J. Process Control.* **2020**, *85*, 76–90. [CrossRef]
2. Liu, G.; Xu, F. Application of robustly adaptive UKF algorithm in ground-based bearings-only tracking for space targets. *Xi Tong Gong Cheng Yu Dian Zi Ji Shu/Syst. Eng. Electron.* **2018**, *40*, 623–629.
3. Bing, Z.; Xu, J.; Miao, W.; Bian, H.; Li, J. Robust adaptive UKF approach for underwater moving base initial alignment. *Yi Qi Yi Biao Xue Bao/Chin. J. Sci. Instrum.* **2018**, *39*, 73–80.
4. Wang, N.; Li, L.; Wang, Q. Adaptive UKF-Based Parameter Estimation for Bouc-Wen Model of Magnetorheological Elastomer Materials. *J. Aerosp. Eng.* **2019**, *32*, 04018130. [CrossRef]
5. Zhang, M.D.; Dai, H.F.; Hu, B.Q.; Chen, C. Robust adaptive UKF based on SVR for inertial based integrated navigation. *Def. Technol.* **2020**, *16*, 846–855. [CrossRef]
6. Li, Y.; Qiao, X.; Wu, H.; Zheng, L.; Zhang, Z. State estimation of distributed electric vehicle based on robust adaptive UKF. *Sci. Sin. Technol.* **2020**, *50*, 1461–1473. [CrossRef]
7. Wang, D.; Zhang, H.; Ge, B. Adaptive Unscented Kalman Filter for Target Tacking with Time-Varying Noise Covariance Based on Multi-Sensor Information Fusion. *Sensors* **2021**, *21*, 5808. [CrossRef] [PubMed]
8. Loukil, J.; Masmoudi, F.; Derbel, N. A real-time estimator for model parameters and state of charge of lead acid batteries in photovoltaic applications. *J. Energy Storage* **2021**, *34*, 102184. [CrossRef]
9. Yuan, H.; Dai, H.; Wei, X.; Ming, P. A novel model-based internal state observer of a fuel cell system for electric vehicles using improved Kalman filter approach. *Appl. Energy* **2020**, *268*, 115009. [CrossRef]
10. Yang, Y.; Li, F.; Gao, Y.; Mao, Y. Multi-Sensor Combined Measurement While Drilling Based on the Improved Adaptive Fading Square Root Unscented Kalman Filter. *Sensors* **2020**, *20*, 1897. [CrossRef] [PubMed]
11. Franchi, M.; Ridolfi, A.; Zacchini, L. 2D Forward Looking SONAR in Underwater Navigation Aiding: An AUKF-based strategy for AUVs. *IFAC-PapersOnLine* **2020**, *53*, 14570–14575. [CrossRef]
12. Hu, G.G.; Gao, B.B.; Zhong, Y.M.; Gu, C. Unscented Kalman filter with process noise covariance estimation for vehicular INS/GPS integration system. *Inf. Fusion* **2020**, *64*, 194–204. [CrossRef]
13. Gan, X.S.; Gao, W.M.; Dai, Z.; Liu, W.D. Research on WNN soft fault diagnosis for analog circuit based on adaptive UKF algorithm. *Appl. Soft Comput.* **2017**, *50*, 252–259.
14. Cheng, J.; Wang, T.; Wang, L.; Wang, Z. A New Polar Transfer Alignment Algorithm with the Aid of a Star Sensor and Based on an Adaptive Unscented Kalman Filter. *Sensors* **2017**, *17*, 2417. [CrossRef] [PubMed]

15. Han, C.; Yang, Y.; Yang, T.; Qin, Y.; Che, Y. Parameter estimation of slow potassium dynamics in a neuron model for seizure-like activity via adaptive lag synchronization and unscented Kalman filter. *Int. J. Mod. Phys. B* **2019**, *33*, 1950159. [CrossRef]

16. Lee, X.Y.; Gao, G.W. An improved algorithm of UKF-SLAM based on RBF neural network adaptive robot. *J. Phys. Conf. Ser.* **2019**, *1325*, 012017. [CrossRef]

17. Peng, S.; Zhu, X.; Xing, Y.; Shi, H.; Cai, X.; Pecht, M. An adaptive state of charge estimation approach for lithium-ion series-connected battery system. *J. Power Sources* **2018**, *392*, 48–59. [CrossRef]

18. Asl, R.M.; Hagh, Y.S.; Palm, R. Robust control by adaptive non-singular terminal sliding mode. *Eng. Appl. Artif. Intell.* **2017**, *59*, 205–217.